CHANNEL FLOW PAST A NEAR-WALL BODY

by F. T. SMITH *and* P. SERVINI[†]

(*Department of Mathematics, University College London, Gower Street, London* WC1E 6BT*, UK*)

Summary

Near-wall behaviour arising when a finite sized body moves in a channel flow is investigated for high flow rates. This is over the interactive-flow length scale that admits considerable upstream influence. The focus is first on quasi-steady two-dimensional flow past a thin body in the outer reaches of one of the viscous wall layers. The jump conditions near the front of the body play an important part in the whole solution which involves an unusual multi-structured flow due to the presence of the body: flows above, below, ahead of and behind the body interact fully. Analytical solutions are presented and the repercussions for shorter and longer bodies are then examined. Second, implications are followed through for the movement of a free body in a dynamic fluid–body interaction. Particular key findings are that instability persists for all body lengths, the growth rate decreases like the 1/4 power of distance as the body approaches the wall, and lift production on the body is dominated by high pressures from an unexpected flow region emerging on the front of the body.

1. Introduction

This study is on dynamic fluid–body interactions in which a body is freely moved by the forces from the surrounding fluid flow and so alters the fluid flow in turn, in a two-way coupling. The body lies initially close to a solid surface or wall. The areas of application are wide-ranging but seem largely untouched by applied mathematics. Many of the application areas involve high Reynolds numbers. The present study is motivated by environmental, industrial and biomedical applications ([1–21]) in principle, but a specific area of interest to us concerns ice shards entering an engine intake ([1], [2], [13]). We note also the intrinsic interest in the fundamental situation of free body movement in surrounding fluid.

More broadly for our readers motivations include sedimentation and fluidisation phenomena, the falling of lumps of ice into an engine intake in an aerodynamic safety context, the travel of wind-blown particles of ice along a wing surface again in the aerodynamic safety context and the falling of rice grains down a chute in a food-sorting context. In addition, various deposition, surface cleansing, plumbing, hoovering and oil-well modelling applications exist for interactions between solid bodies and fluids. There are also biomedical applications in travel of solids within vessels of major networks in the human body such as transport of blood clots, embolisation procedures in stroke treatment (transportation of glue) and drug-delivery to tumours. Experimental and computational works in the area include ([3–9]). More analytically based works investigating the mechanics involved

---

[†]<pietro.servini@gmail.com>

at high flow rates are in (**1**, **2**, **10**–**16**) mostly on inviscid fluids, the exceptions being in (**1**, **2**). There is also application to branching flows affected by substantial oncoming vorticity and by pressure conditions downstream of the branching (**22**, **23**).

In dynamic fluid–body interactions, there is a multi-parameter space with which to contend. Included in it are the typical Reynolds number and Mach number and, for a single body say, the ratio of body density to fluid density, the Stokes number, the body shape, initial location, thickness factors, orientation, mass, moment of inertia, position of centre of gravity as well as extra factors for a three-dimensional body. The space can also increase in size considerably if more than one body is involved.

Recent theoretical studies (**1**, **2**) of dynamic interactions for weakly viscous incompressible fluids and thin bodies have highlighted three particular points especially. These points are: the substantial influence of a so-called Euler zone, very close to the leading edge of the body, in which the oncoming fluid motion is adjusted significantly in anticipation of the overall flow past the body; the differences in mechanisms between interactions for short bodies, where inviscid effects are paramount in the pressure forces, and long bodies where feedback from viscous wall layers is considerable; and the need for increased understanding of the steady flow past a fixed thin finite body as a pre-cursor to investigating temporal evolution. Concerning the last point, the body movement then responds to the pressure forces from the fluid flow, leaving the flow itself as quasi-steady. This typically involves an assumption that the body is considerably denser than the fluid. Complex flow structure is present for both the shorter and the longer types of body. Similar considerations apply again to the context of branching flow, and to reconnecting flows, although here the focus is mostly on the setting of a finite sized body in surrounding fluid flow. Further, the recent studies of fluid–body coupling show that unusual temporal growth or instability arises for relatively short or long length scales outside the conventional range of flow instability.

The present study for high Reynolds numbers also includes significant effects from viscosity and hence vorticity. This is in two spatial dimensions. The study is for a thin finite body which is nearly aligned axially within a channel flow, with the channel having straight parallel walls. An example of the incident flow is plane Poiseuille flow. We consider a body that is short compared with the development length of the channel flow and the body is situated in the relatively thin viscous-inviscid layer near one wall, in contrast with (**1**, **2**). The ratio of the body chord in the axial direction to the channel width is however large, of the order of the Reynolds number Re to the power 1/7 and we assume the majority of the flow response is over the same length scale.

The reasons for considering the 1/7 case (**24**) are that it involves a full viscous-inviscid interplay, between the inviscid core flow holding across most of the channel and the viscous layers near the walls; it thereby accounts for the predominant upstream influence ahead of the body; and it is expected to provide a crossover from the shorter-body cases (**1**) to the longer-body cases (**2**), giving a check on each type. Such a crossover is known to occur in the effects of shorter and longer scale constrictions in channel flow (**25**). In addition, the work (**1**) on comparatively short bodies raises serious questions about the behaviour and assumptions made over longer length scales: the short-scale response which is mainly inviscid was found to be intimately coupled with the viscous-inviscid response on the longer 1/7 scale. Likewise the work (**2**) concerning comparatively long bodies raises substantial issues over the influence from active shorter length scales near the leading edge (which comprise the 1/7 length scale and a shorter Euler zone), again suggesting the desirability of checking through a matching process. Given that there are many parameters, we explore the dependence on body length and position. The latter is close to the wall now, contrasting with (**1**, **2**). Smith (**2**) examined effects

independent of the lateral position, whereas we may expect positional dependence to emerge close to the wall. Finally, here the 1/7 case also accounts for pure channel flow instability as in (**26**). It is thus a central case in several senses.

The presence of a detached body within the otherwise well-established 1/7 flow structure causes delicate new features to arise. The body is taken as if fixed at first and the surrounding flow is assumed quasi-steady and two-dimensional, bearing in mind the points above, with unsteadiness being accommodated subsequently. We aim to understand the structure of the flow in detail and the implications for shorter and longer bodies where quite distinct mechanisms come into action. The influence of the Euler zone is found to be crucial in a multi-structure in which the flows above and below the body are linked through asymptotic matching with the flows upstream, near the leading edge and in the wake. Gaining insight is thus a challenge.

We use non-dimensional Cartesian coordinates x_N axially and y_N laterally with corresponding velocity components u_N and v_N, respectively and pressure variation p_N, these quantities being based on the channel width a_D, typical oncoming velocity u_D in the channel and the density and the kinematic viscosity ν_D of the fluid where the subscript D denotes a dimensional quantity. The Reynolds number $\text{Re} = u_D a_D / \nu_D$ is large. The upstream end of the thin nearly aligned body located inside a viscous wall layer is the leading edge and the rear is the trailing edge. Section 2 describes the rather intricate set-up of concern. This leads to a nonlinear viscous-inviscid flow problem in which solution discontinuities or jumps across the comparatively small Euler zone near the leading edge station play a full part together with mixed boundary conditions. These conditions are of pressure–displacement interactive form upstream and downstream but of prescribed displacement form between the leading and trailing edges. Section 3 discusses the situation when the body is in the outer reaches of the wall layer, where much more analytical progress is possible. Due to the jumps, two axial length scales appear along with a new interaction. Our aim is to understand basic effects of position, length and thickness of the body. For that reason a linearised approach is used and detailed solution properties are examined in sections 4 and 5 in turn. Section 6 investigates the role of body length in the flow solutions, followed by section 7, which is on the implications for free unsteady motion of the body. Conclusions are presented in section 8, while a range of practical examples is discussed in Appendix A and certain numerical details are given in Appendix B. Major findings are instability persisting for all body lengths in the fluid–body interaction and the lift being dominated by high-pressure effects over the short axial length scale at the leading edge.

2. Nonlinear flow structure

The undisturbed flow in the straight channel far upstream and downstream is essentially uni-directional in the axial direction with a velocity profile $u_N = U_0(y_N)$ that is zero at the walls $y_N = 0, 1$ and positive in between. The interactive flow of interest here mainly has the long axial scaling $x_N = \text{Re}^{1/7} x$ with x of $O(1)$ as described in subsection 2.1. However, this is supplemented by a relatively small region due to the presence of the body (see Fig. 1), which is discussed in subsection 2.2, where jump discontinuities across that region are found to exert a controlling influence on the entire motion. Subsection 2.3 then summarizes the flow problem.

2.1 *The long-scale structure*

The flow structure comprises three primary regions, a predominantly inviscid core and a thin viscous (or viscous-inviscid) layer near each wall $y_N = 0, 1$: this is from (**24**, **25**) but supplemented by a

(a)

(b)
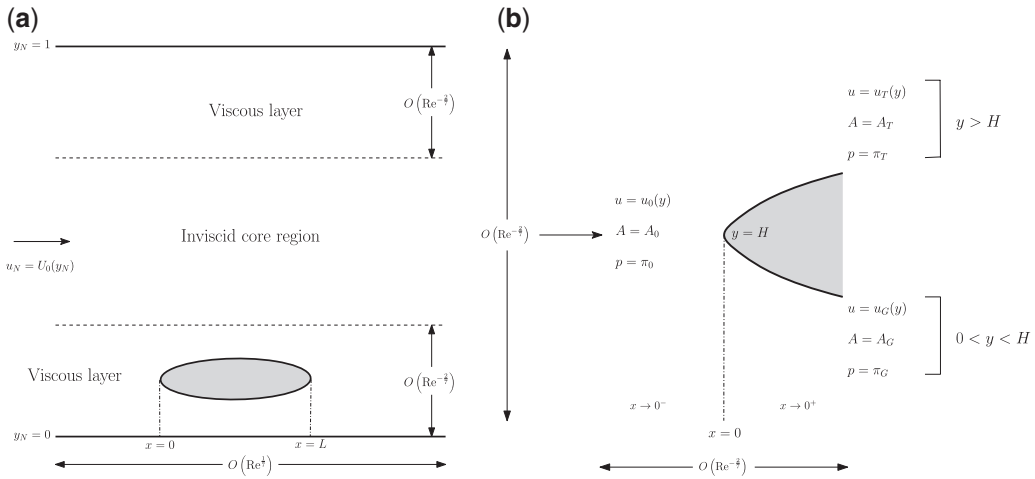
Fig. 1   Sketch of the flow structure with a thin body present inside the near-wall sublayer in a straight channel flow. The zones for: (a) the $O(\text{Re}^{1/7})$ length scale of the main upstream influence; and (b) for the shorter $O(1)$ and $O(\text{Re}^{-2/7})$ length scales of leading edge adjustment or Euler flow behaviour are shown. The diagram is in non-dimensional terms and not to scale.

relatively small region due to the presence of the body (see Fig. 1). The flow solution expands in the form

$$(u_N, v_N, p_N) = \left(U_0\left(y_N\right) + \text{Re}^{-2/7}A\left(x\right)U_0'\left(y_N\right), \right.$$
$$\left. -\text{Re}^{-3/7}A'\left(x\right)U_0\left(y_N\right), \text{Re}^{-4/7}p_{\text{core}}\left(x, y_N\right) \right) + \cdots \qquad (2.1a)$$

in the core where y_N is of $O(1), 0 < y_N < 1$, whereas in the lower and upper wall layers $y_N = \text{Re}^{-2/7}y$, $y_N = 1 - \text{Re}^{-2/7}\hat{y}$, respectively with $y, \hat{y}$ of $O(1)$ and the expansions applying are

$$(u_N, v_N, p_N) = \left(\text{Re}^{-2/7}u, \text{Re}^{-5/7}v, \text{Re}^{-4/7}p(x) \right) + \cdots, \qquad (2.1b)$$

$$(u_N, v_N, p_N) = \left(\text{Re}^{-2/7}\hat{u}, -\text{Re}^{-5/7}\hat{v}, \text{Re}^{-4/7}\hat{p}(x) \right) + \cdots, \qquad (2.1c)$$

in turn. In (2.1a), we have anticipated that the core motion is simply displaced from the incident motion by an amount $-A(x)$ in scaled terms and that the wall pressures $p, \hat{p}$ as well as A are unknown functions of x. The core pressure p_{core} which is y-dependent from the nontrivial normal momentum balance in the core is equal to $p(x), \hat{p}(x)$ at $y_N = 0, 1$, respectively.

The thin body is assumed to be located exactly inside the lower wall layer as in Fig. 1, that is, its length is of order $\text{Re}^{1/7}$ and its representative height and thickness (in y_N) are of order $\text{Re}^{-2/7}$. For convenience we also take the scaled wall shear stresses $U_0'(0), -U_0'(1)$ at $y_N = 0, 1$ to have the same value, denoted by λ which is positive. The nonlinear case of current concern is thus governed by the following system. First, in the lower viscous layer from substitution of (2.1b) into the Navier–Stokes

equations we have the boundary-layer equations with associated conditions as follows:

$$u_x + v_y = 0, \quad uu_x + vu_y = -p'(x) + u_{yy}, \tag{2.2a}$$

$$u = v = 0 \text{ at } y = 0 \text{ and at } y = F^{\pm}(x), \tag{2.2b}$$

$$u \sim \lambda \, (y + A) \text{ as } y \to \infty, \tag{2.2c}$$

Euler jump conditions across the leading edge $x = 0^{\pm}$, $\qquad$ (2.2d)

A Kutta condition of equal pressures at the trailing edge $x = L$, $\qquad$ (2.2e)

Boundedness upstream and downstream as $x \to \pm\infty$. $\qquad$ (2.2f)

In (2.2a), the prime denotes the straight derivative with respect to x and the pressure is independent of y by virtue of the normal momentum balance. The condition (2.2b) imposes zero slip on the solid fixed surfaces present, namely the channel wall and the underbody and overbody given by the positive functions $F^{\pm}(x)$ between 0, L, with $F^{+}(x) > F^{-}(x)$ for $0 < x < L$, $F^{+}(0) = F^{-}(0)$ for a definite leading edge and similarly $F^{+}(L) = F^{-}(L)$ at the trailing edge. The corresponding stream function ψ, defined by $u = \partial\psi/\partial y$, $v = -\partial\psi/\partial x$ subject to $\psi = 0$ at the wall $y = 0$, is equal to an unknown constant on the body surface. Matching with the core flow is ensured by (2.2c), while the requirement in (2.2d) is considered in detail in the next subsection and that in (2.2e) is the standard trailing edge constraint for attached flow. The boundedness in (2.2f) broadly means that no exponential growth is admitted far upstream or downstream. Second, in the upper viscous layer we have the same equations and constraints applying for $\hat{u}, \hat{v}, \hat{p}$ in terms of $x, \hat{y}$ except that:

$$\hat{u} \sim \lambda \, (\hat{y} - A) \text{ as } \hat{y} \to \infty; \tag{2.2g}$$

there is no body present and so the counterpart of (2.2b) simply requires zero $\hat{u}, \hat{v}$ at $\hat{y} = 0$; and there is no Euler jump or Kutta condition in the upper layer. Third, the pressure–displacement law

$$p(x) - \hat{p}(x) = -JA''(x) \tag{2.2h}$$

holds for the wall pressures except in the gap between the body and the lower channel wall. The constant J is the integral of $U_0(y_N)^2$ in y_N from zero to unity; $J = 1/30$ in the case of plane Poiseuille flow where $U_0(y_N) = y_N(1 - y_N)$. The body occupies $0 < x < L$ and is detached from the wall, where L of order unity is the scaled body length, while the scaled gap width or height $F^{\pm}(0)$ of the leading edge is denoted H, where H is generally of order unity. The constant J and the skin friction factor λ are positive and of $O(1)$; they could be normalised to unity in the current problem but it is clearer to retain their presence explicitly throughout from the viewpoint of seeing their effects on the solution properties.

Upstream influence is present (24) in an eigenform in which, at large negative x values, $u - \lambda y$ is proportional to $\exp(\kappa x)$ with a known positive constant κ. The upstream influence implies we have nontrivial features $(p(x), u(x, y), A(x)) = (\pi_0, u_0(y), A_0)$ at $x = 0^-$, with the pressure constant π_0 to be found. Here, the velocity profile $u_0(y)$ is nontrivial but satisfying $u_0(0) = 0$ and $u_0(y) \sim \lambda(y + A_0)$ at large $\hat{y}$. The negative displacement contribution A_0 depends on π_0 in a known way (24).

2.2 *The Euler flow region and the jump discontinuities across it*

The Euler jump stems from properties of the small Euler region of extent $O(\mathrm{Re}^{-2/7})$ in both x_N, y_N that surrounds the leading edge of the body. Here, the Euler equations govern the velocity components,

which are $O(\mathrm{Re}^{-2/7})$ and the pressure which is $O(\mathrm{Re}^{-4/7})$ locally, and tangential flow constraints hold on the solid surfaces present. Thus the relevant local expansion for y of $O(1)$ but $x_N = \mathrm{Re}^{-2/7} x_E$ with x_E of $O(1)$ is

$$(u_N, v_N, p_N) = \left(\mathrm{Re}^{-2/7} u_E, \mathrm{Re}^{-2/7} v_E, \mathrm{Re}^{-4/7} p_E\right) + \dots. \tag{2.3}$$

This gives the quasi-steady Euler equations for the unknown velocity components and pressure,

$$\frac{\partial u_E}{\partial x_E} + \frac{\partial v_E}{\partial y} = 0, \tag{2.4a}$$

$$u_E \frac{\partial u_E}{\partial x_E} + v_E \frac{\partial u_E}{\partial y} = -\frac{\partial p_E}{\partial x_E}, \tag{2.4b}$$

$$u_E \frac{\partial v_E}{\partial x_E} + v_E \frac{\partial v_E}{\partial y} = -\frac{\partial p_E}{\partial y}, \tag{2.4c}$$

to leading order. Cross-differentiation of (2.4b, 2.4c) to eliminate p_E then shows that the scaled vorticity $(\partial v_E/\partial x_E - \partial u_E/\partial y)$ is conserved along the unknown streamlines, while addition of the x_E-derivative of (2.4b) to the y-derivative of (2.4c) shows conservation of the Bernoulli pressure head $(p_E + (u_E^2 + v_E^2)/2)$ holds along the streamlines. Hence in terms of the scaled stream function ψ_E defined by $u_E = \partial \psi_E/\partial y$, $v_E = -\partial \psi_E/\partial x_E$, with ψ_E set to zero at the lower channel wall without loss of generality, (2.4a)–(2.4c) yields the conservation equation

$$\left(\frac{\partial^2}{\partial x_E^2} + \frac{\partial^2}{\partial y^2}\right) \psi_E = f_E(\psi_E), \tag{2.5}$$

in particular, where f_E denotes the negative vorticity in scaled variables.

Concerning the boundary conditions and matching for the Euler flow, substantive changes can occur (10–16, 22) between the incoming flow upstream (scaled pressure $p = \pi_0$, velocity $u = u_0(y)$, displacement A_0) and the outgoing flow downstream. The changes produce pressure $p = \pi_G$, velocity $u = u_G(y)$ at $x = 0^+$ in the gap, that is, for $0 < y < H$, and pressure $p = \pi_T$, velocity $u = u_T(y)$, displacement A_T at $x = 0^+$ on top of the body where $y > H$ (see Fig. 1b). These changes have to be consistent with the conservation of vorticity and pressure head along the streamlines of the Euler flow field described above. Physical reasoning based on the local length and pressure scales also leads to the additional requirement that

$$A_T = A_0 \tag{2.6}$$

since the length scales local to the leading edge jump effects are short and so condensed-flow theory (25, 27) applies there. In brief, if the displacement is discontinuous then the pressure response that is produced is too large to be sustained by the local flow structure; hence (2.6) follows. The requirement (2.6) acts to determine π_T as a function of π_G for given incoming conditions $(\pi_0, u_0(y), A_0)$. Moreover, the jump condition in the gap yields

$$\pi_G + \frac{1}{2} u_G (0^+)^2 = \pi_0, \tag{2.7}$$

from the Bernoulli pressure head with the assumption that $\pi_G < \pi_0$. The initial profile $u_G(y)$ for the gap at $x = 0^+$ has nonzero slip in general: the slip is smoothed out at small positive x within an
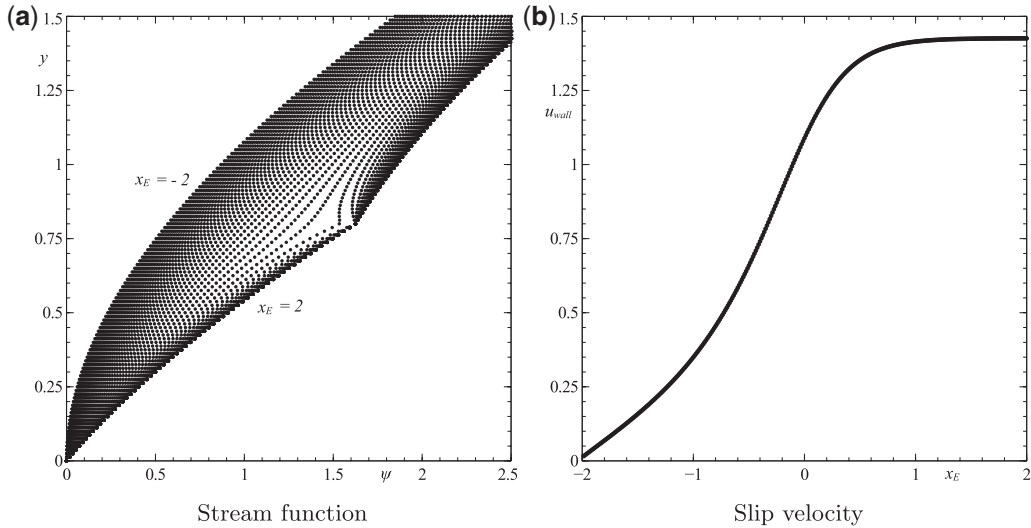
Fig. 2 Numerical solution of Euler flow showing (a) profiles of the scaled stream function at various x_E stations, (b) the scaled slip velocity u_{wall} produced at the wall, versus x_E. Here, the incoming flow has velocity profile $u_0 = y + 1 - \exp(-y)$, pressure $\pi_0 = 1.2$; the outgoing pressure in the gap is $\pi_G = 0.2$; the body is given by $y = H = 0.8$ for x_E positive.

$O(x^{1/2})$ sublayer at the wall. Similarly, there are $O(x^{1/2})$ sublayers for small x on either face of the body.

A sample solution for the Euler flow region is shown in Fig. 2 based on solving the conservation form (2.5). Here, the negative vorticity f_E is determined by the incident velocity profile $u_0(y)$ applying at large negative x_E values: thus $f_E = du_0/dy$ in effect. Further details are presented in Appendix B. Figure 2a shows the stream function profiles, while Fig. 2b presents the corresponding slip velocity variation $u_{wall} = \partial\psi_E/\partial y$ induced at the wall. The prescribed pressures p_E upstream and downstream are $\pi_0 = 1.2$ and $\pi_G = 0.2$ in turn, the slip velocity increases in the axial direction and the pressure gradient is favourable throughout implying that the thin boundary layer at the wall remains attached. The decay into the incident conditions upstream is algebraic, whereas that downstream entering the gap is exponential.

Numerical solutions for the inferred features holding at $x = 0^+$ are presented in Fig. 3. They were obtained as follows. Given the incident velocity profile $u_0(y)$, the corresponding stream function $\psi = \psi_0(y)$ is evaluated by integration of $u_0(y)$ in y subject to $\psi_0(0)$ being zero. Hence the conservation properties along streamlines through the Euler zone yield the relation that if the value of the height Y at $x = 0^+$ is associated with the streamline emanating from height y at $x = 0^-$ then $u_G(Y) = (u_0(y)^2 - 2\pi_{diff})^{1/2}$ gives the velocity profile at that height, where $\pi_{diff} = \pi_G - \pi_0$ is the pressure difference across the Euler zone. The above is for streamlines that enter the gap beneath the body. So since $d\psi_0/dY = u_G(Y)$ we have $dY/d\psi_0 = (u_0(y)^2 - 2\pi_{diff})^{-1/2}$, from which the result

$$dY/dy = u_0(y)/\left(u_0(y)^2 - 2\pi_{diff}\right)^{\frac{1}{2}} \tag{2.8a}$$
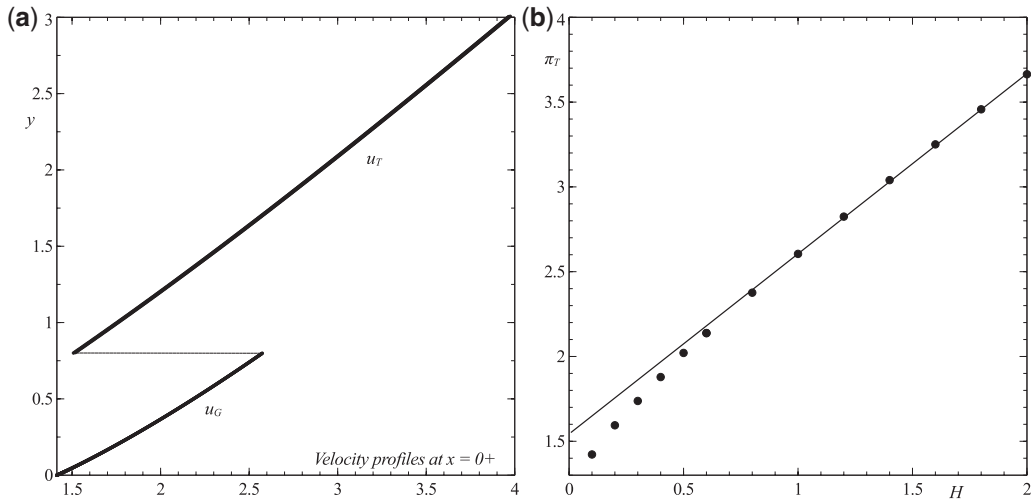
Fig. 3 (a) Solution for the velocity profiles induced at the beginning of the gap (u_G) and beginning of the flow on top of the body (u_T), given the incoming flow and pressure values of Fig. 2 with $H = 0.8$. (b) The pressure response π_T versus gap width H for fixed pressures $\pi_0 = 1.2$, $\pi_G = 0.2$ and displacement $A_0 = 1$; dotted, numerical results; solid, asymptote for H large.

follows. (We suppose π_{diff} is negative. See (**28**) on attached and separating flows in the gap.) The result together with Y being zero at the lower wall, consistent with (2.4), enables Y to be calculated successively for each streamline by integration in increasing y. When the calculated Y passes through the value H where the leading edge closes off the gap then the same result (2.8a) applies but with π_{diff} replaced by $\pi_{\text{diff}} = \pi_T - \pi_0$. The velocity profile becomes $u_T(Y)$ which in general is not continuous with $u_G(Y)$ at $Y = H$ owing to the pressure differences. At large y and hence large Y, the profile u_T takes on a displaced form because of the nature of the incident profile. The results in Figs 2 and 3 take a representative incident velocity profile $u_0(y)$, namely $y + A_0(1 - \exp(-y))$, pressure π_0 of 1.2 and displacement A_0 of 1, a particular value 0.2 for π_G, and the results then cover a range of heights H. Figure 3a presents the velocity profile for H of 0.8 and the π_T value iterated in order to satisfy the local displacement criterion (2.6), while Fig. 3b gives the solutions π_T that satisfy the criterion (2.6) as the height H is varied. The profile discontinuity on crossing the height $y = H$ and the effective displacement at increased y are clear. As H increases a linear trend in π_T is suggested by the computations.

Analytically two scales emerge in the y coordinate when H is large, one for y of $O(1)$ where the curved profile of $u_0(y)$ has leading-order influence and leaves u_G growing as $\lambda(y + A_G)$ as y increases and the other for y of $O(H)$ where $u_0(y)$ has uniform shear and hence $u_G(y)$ is identically $\lambda(y + A_G)$ in effect. For y below H the pressure π_G is $O(1)$ and the stream function $\psi_2(y)$ is $(1/2)\lambda(y + A_G)^2 + c_2$ with c_2 an $O(1)$ constant. Above $y = H$ similarly we have $u_T(y)$ as $\lambda(y + A_T)$, $\psi_1(y)$ as $(1/2)\lambda(y + A_T)^2 + c_1$ with c_1 a constant but the pressure π_T is to be determined so as to make A_T equal to A_0 from (2.6). On the body at $y = H$, continuity of ψ then requires $H(A_G - A_0) + (1/2)(A_G^2 - A_0^2) = (c_1 - c_2)/\lambda$, whereas the Bernoulli balance requires $(\pi_T - \pi_G)/\lambda^2 = H(A_G - A_0) + O(1)$. So, since

π_G is of order unity, we obtain the relation

$$\pi_T = \lambda^2 (A_G - A_0) H + \cdots , \text{ at large } H. \tag{2.8b}$$

In numerical terms A_G is approximately 2 for the case where $(A_0, \lambda, \pi_0, \pi_G) = (1, 1, 1.2, 0.2)$, leading to a slope of approximately 1 for $d\pi_T/dH$ from (2.8b). Figure 3b indicates that this asymptotic slope agrees with the trend in the computational results, and indeed the latter are close to the asymptotic form for H values above about unity.

The jump results described above are for the lower viscous layer. There is no such jumping in the upper layer because no solid body surface is present there to support the corresponding pressure changes. Hence $\hat{p}, A$ are continuous across $x = 0^\pm$. So owing to the relation (2.2h) the change in p near the lower wall yields the requirement $\pi_T - \hat{p}(0) = -JA''(0^+)$ from which we can infer that A, A' are continuous but A'' is discontinuous in general across the $x = 0$ station.

2.3 *Summary of the fluid–body interaction problem*

The pressures in the lower viscous layer above and below the body over the range $0 < x < L$ are written $p = p_{\text{top}}(x), p_{\text{gap}}(x)$, with $p_{\text{top}}(0^+), p_{\text{gap}}(0^+)$ equal to π_T, π_G, respectively. The Kutta condition then requires, with the starting values π_T, π_G affecting $p_{\text{top}}(x), p_{\text{gap}}(x)$, respectively throughout $0 < x < L$, the pressure balance

$$p_{\text{gap}} = p_{\text{top}} \text{ at } x = L. \tag{2.9}$$

We assume p to be streamwise continuous across the trailing edge station. Further downstream,

$$p(+\infty) = \hat{p}(+\infty) = 0 \tag{2.10}$$

gives the boundedness requirement in general. In summary our task is to solve the problem (2.2), (2.6)–(2.10) that governs the interaction over the long length scale involved.

Counting the independent unknown constants, we have in effect two, namely the pressures π_0, π_G. Counting the conditions remaining to be satisfied, we also have two, namely (2.9), (2.10). A forward march in x from $x = 0^+$ with a guessed pair of values π_0, π_G followed by using the two conditions (2.9), (2.10) to determine updates of the pair, with iteration, seems a feasible calculation approach. As part of this we can expect the scaled stream function ψ in the lower layer to be equal to an unknown constant on the body surface. It is apparent however that the nonlinear problem (2.2), (2.6)–(2.10) as it stands is a hard numerical one in general. A vital point here is that linearisation is not valid for $O(1)$ values of the parameters λ, L, H and for $O(1)$ stations x even if the body is relatively thin. Yet, we believe that analytical progress is essential to understanding, especially in the current intricate situation. With that in mind, we move on to explore the roles of position, length and thickness of the body.

3. Large H nonlinear cases: effects of body position

The body is now taken to be initially in the upper reaches of the viscous wall layer. Thus we seek insight for cases where the typical scaled body height from the wall is large, so that the gap is enlarged between the lower wall and the body. The flow structure for (2.2), (2.6)–(2.10) when $H \gg 1$ is interesting, especially in view of the behaviour suggested by the trend found in Fig. 3b.

The main x scale remains of $O(1)$, but we can immediately anticipate another x scale also emerging as H increases: this is the short length scale $H^{-1/2}$ over which the large pressure of order H on the left-hand side of (2.2h) is balanced by the curvature term due to displacement of order unity from (2.6). The body inside the lower viscous layer is sited now at $y = F^{\pm}(x) = Hy_0^* + O(1)$, where the constant $y_0^* = 1$ but is retained in the working to keep track of the height effect. We will concentrate primarily then on this lower viscous layer and its structure, whereas the viscous layer at the upper wall remains largely as in the previous section.

When H is large we expect five sublayers 1–5 to occur for the interval $0 < x < 1$ as depicted in Fig. 4 and studied in subsections 3.1–3.5 below. Sublayer 1 is a viscous sublayer near the channel wall, sublayer 2 is an essentially inviscid sublayer between the wall and the underbody, while sublayer 5 is the quasi-inviscid sublayer above the body and sublayer 3 represents the comparatively thin viscous sublayers on the body itself. The extra sublayer 4 is that anticipated in the previous paragraph, lying on top of the body over a short axial length scale. We can also expect the Euler jump conditions to produce merely a displacement of the incident velocity profile $u_0(y)$ for most positive y values but combined with an over-body pressure π_T that is of order H,

$$\pi_T = H\pi_T^*, \tag{3.1}$$

say to leading order: see the computational results in Fig. 3. In contrast, the local incident and gap pressures π_0, π_G, respectively are expected to remain $O(1)$. The five sublayers are addressed in turn below.

3.1 *Sublayer 1*

Sublayer 1 has flow quantities of order unity throughout, hence being subjected to the leading order-unity effects $(\pi_0, u_0(y), A_0)$ from the upstream region and from the leading edge jump directly, such that

$$(u, \psi, p) = (u_1, \psi_1, p_1) + \cdots, \quad y = O(1), \tag{3.2}$$

with $x \sim 1$. It follows that the boundary-layer equations (2.2a) continue to hold in full for the subscripted quantities in terms of x, y. The relevant boundary conditions are
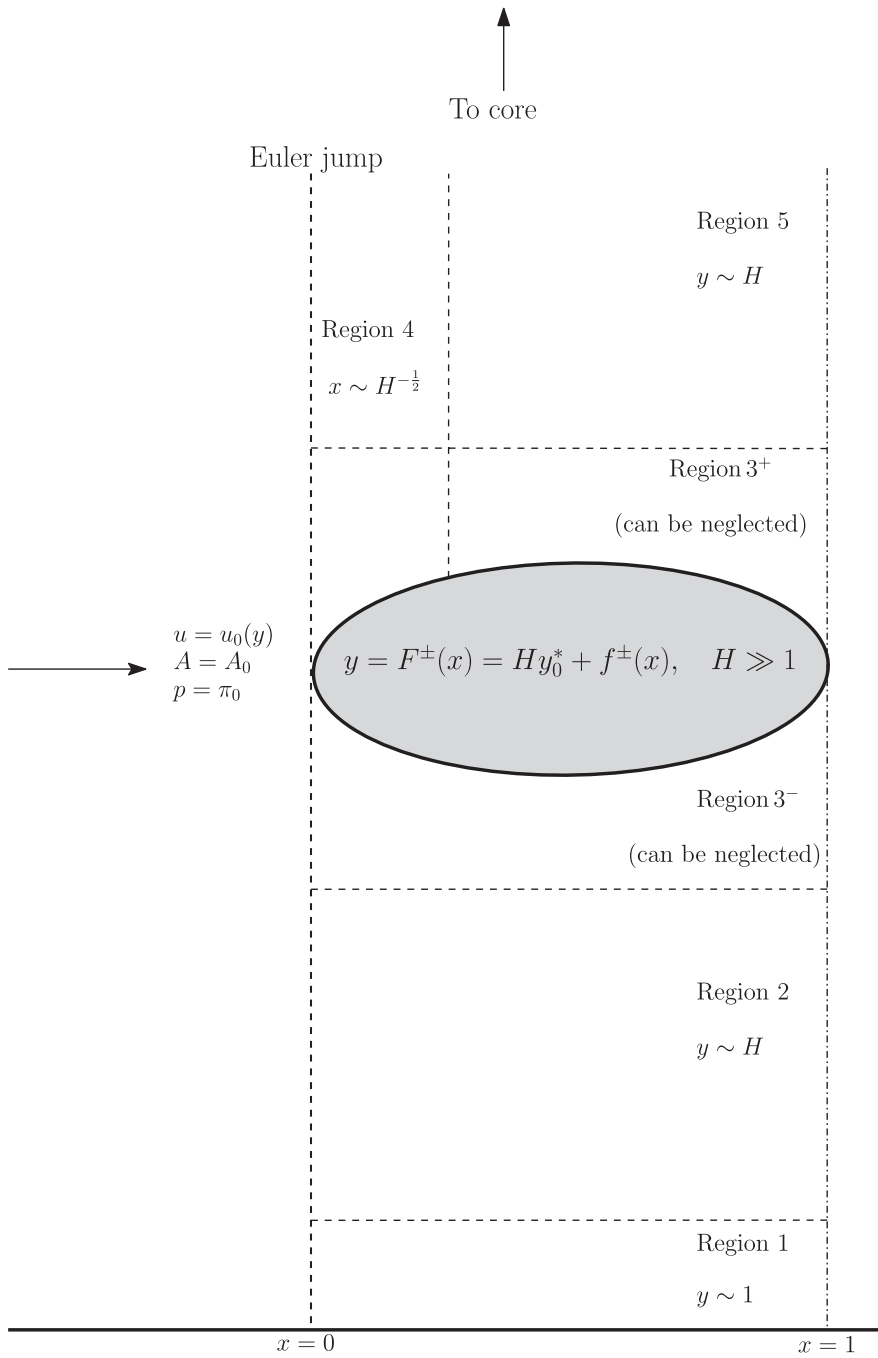
$$u_1 = v_1 = 0 \text{ at } y = 0, \tag{3.3a}$$

$$u_1 \sim \lambda \left(y + A_2(x)\right) \text{ as } y \to \infty, \tag{3.3b}$$

$$u_1 \left(x = 0^+\right) = u_G(y) \text{ for all } y > 0, \quad p_1 \left(x = 0^+\right) = \pi_G, \tag{3.3c}$$

where vorticity u_y is conserved along Euler streamlines (recalling subsection 2.2), (2.7) holds and the unknown profile $u_G(y)$ and pressure π_G are as in section 2. The unknown displacement $A_2(x)$ is inferred from the large-H results in Fig. 3 and also anticipates the displacement effect found below in sublayer 2 lying on top of the present sublayer. If we know π_G we can determine $u_G(y)$ for $0 < y < \infty$ from the Euler jump. As $y \to \infty$ the velocity profile $u_G(y)$ behaves as $\lambda(y + A_2(x = 0^+))$, a displacement form.

3.2 *Sublayer 2*

Sublayer 2 is relatively thick and quasi-inviscid, occupying the gap between the underside of the body and the top of sublayer 1. In sublayer 2, we have $y = Hy^*$ with y^* of order unity. The dominant

To core

Euler jump

Region 5

$y \sim H$

Region 4

$x \sim H^{-\frac{1}{2}}$

Region 3^+

(can be neglected)

$u = u_0(y)$
$A = A_0$
$p = \pi_0$

$y = F^{\pm}(x) = Hy_0^* + f^{\pm}(x), \quad H \gg 1$

Region 3^-

(can be neglected)

Region 2

$y \sim H$

Region 1

$y \sim 1$

$x = 0$ $\qquad$ $x = 1$

Fig. 4 Flow structure when the scaled height H of the body is relatively large, indicating regions 1–3, 5 on the length scale x of order unity and the additional region 4 over the shorter length scale x of order $H^{-1/2}$. The structure concerns the effects of body position and thickness.

displacement effect here follows from properties of the Euler zone solution as explained in section 2. Here y^* is of order unity with $0 < y^* < y_0^*$ and

$$(u, \psi, p) = \left(\lambda H y^* + u_2, \lambda H^2 y^{*2}/2 + H\psi_2, p_2\right) + \cdots, \tag{3.4}$$

where the governing equations (2.2a) yield the solutions

$$u_2 = \lambda A_2(x), \tag{3.5a}$$

$$\psi_2 = \lambda A_2(x)y^* \tag{3.5b}$$

with

$$A_2(0^+) = A_G. \tag{3.5c}$$

Boundary and matching conditions require $p_2 = p_1(x)$, while the match with the velocity response in sublayer 1 as $y^* \to 0^+$ is as displayed earlier in (3.3b), and tangential flow on approach to the underbody as $y^* \to y_0^{*-}$ requires

$$A_2(x) = -f^-(x) - K^-. \tag{3.5d}$$

Here f^- is the scaled underbody shape such that $F^\pm(x) = Hy_0^* + f^\pm(x)$ and K^- is a constant to be found representing the unknown mass flux into the gap. We take the finite body shape as closed such that $f^+(0) = f^-(0)$ at the leading edge and similarly $f^+(L) = f^-(L)$ at the trailing edge.

3.3 Sublayer 3

Sublayer 3 consists of attached Blasius layers, one on each side of the body. Their thickness is much less than that of the body and their influence on the current interactions is negligible.

3.4 Sublayer 4

The apparently straightforward fluid–body interaction now yields more subtlety as the regions above the body involve an extra length scale. In fact there is a precursor sublayer 4 at small x directly ahead of sublayer 5. Within sublayer 4 we have $x = H^{-1/2}x^*$ with x^* of $O(1)$ and the expansion

$$(u, \psi, p) = \left(\lambda H y^* + u_4, \lambda H^2 y^{*2}/2 + H\psi_4, Hp_4\right) + \cdots, \tag{3.6}$$

holds for order-unity values of $y^* > y_0^*$. We notice that the displacement is $O(1)$ in this sublayer, namely $-A_4$ as described below, whereas the pressure has been raised (to combat the displacement over the present enlarged gap in effect) to order H in keeping with the trend (3.1). The controlling equations here are

$$u_4 = \partial\psi_4/\partial y^*, \tag{3.7a}$$

$$\lambda y^* \left(\partial u_4/\partial x^*\right) - \left(\partial\psi_4/\partial x^*\right)\lambda = -\mathrm{d}p_4/\mathrm{d}x^*, \tag{3.7b}$$

from substitution into (2.2a). The presence of the pressure gradient in the streamwise momentum balance at leading order is noteworthy. The solution is therefore

$$u_4 = \lambda A_4 \left(x^*\right), \tag{3.8a}$$

$$\psi_4 = \lambda A_4 y^* + p_4/\lambda. \tag{3.8b}$$

The boundary conditions here yield

$$A_4 \left(x^*\right) = \left[\pi_T^* - p_4 \left(x^*\right)\right] / \left(\lambda^2 y_0^*\right) - f^+ \left(x^*\right) - K^+, \tag{3.8c}$$

$$A_4 \left(0^+\right) = A_0, \tag{3.8d}$$

bearing in mind that we expect $p_4(0^+) = \pi_T^*$ because of the jump conditions. The original displacement function expands in the form $A = A_4 + \cdots$ over the present length scale, giving an $O(1)$ displacement. The scaled overbody shape f^+ on the present short scale of x^* in fact remains as a constant for most reasonably shaped bodies, even though it may vary considerably over the longer length scale, and the unknown constant K^+ again corresponds with a mass flux to be determined. The scaled pressure–curvature balance

$$p_4 \left(x^*\right) = -J d^2 A_4 / dx^{*2} \tag{3.8e}$$

also applies in view of (2.2h) and the largeness of the pressure response here compared with that in the upper wall layer. Combining (3.8c)–(3.8e) and recognising that f^+ is effectively constant over the current short scale of x^* we then obtain the ordinary differential equation

$$d^2 p_4 / dx^{*2} = \lambda^2 y_0^* J^{-1} p_4 \tag{3.9}$$

for the scaled pressure. The appropriate solution is simply

$$p_4 = \pi_T^* \exp \left(-q^* x^*\right), \tag{3.10a}$$

since x^* is positive and a growing exponential is inadmissible. Here the positive constant $q^* = (\lambda^2 y_0^* J^{-1})^{1/2}$ is given. The associated displacement is thus, from (3.8c),

$$A_4 \left(x^*\right) = \pi_T^* \left[1 - \exp \left(-q^* x^*\right)\right] / \left(\lambda^2 y_0^*\right) - f^+(0) - K^+. \tag{3.10b}$$

Hence the starting condition at $x = 0^+$ leads to the value

$$K^+ = -A_0 - f^+(0), \tag{3.10c}$$

where, to repeat, A_0 is the incident displacement due to upstream influence. Also from (3.10b) we have the result

$$A_4(\infty) = \pi_T^* / \left(\lambda^2 y_0^*\right) - f^+(0) - K^+, \tag{3.10d}$$

at downstream infinity on the current scale. A plot of the scaled pressure and displacement solutions within sublayer 4 is given in Fig. 5. We observe that the pressure falls or rises monotonically to zero as x^* tends to infinity downstream, given π_T^* positive or negative, respectively.
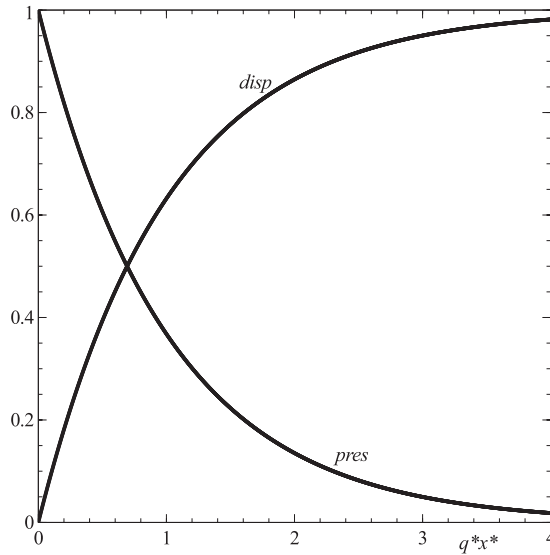
Fig. 5 Scaled pressure and relative displacement versus axial distance in the local region 4 near the leading edge on the upper body, plotted, respectively as p_4/π_T^* (denoted *pres*) and $(A_4 - A_0)/\pi_T^*$ (denoted *disp*) against q^*x^*. Here, λ, y_0^* are taken as unity, π_T^* is the pressure-jump effect in (3.1) and A_0 is the upstream displacement effect in section 2.

3.5 *Sublayer 5*

Sublayer 5 follows on from sublayer 4 as x becomes $O(1)$. The expansion now has the form

$$(u, \psi, p) = \left(\lambda Hy^* + u_5, \lambda H^2 y^{*2}/2 + H\psi_5, p_5\right) + \cdots . \tag{3.11}$$

Here y^* is again of order unity, while crucially the pressure p is reduced to $O(1)$ again and the displacement ($A = A_5 + \cdots$) is also of $O(1)$. The solution response has a pure displacement,

$$u_5 = \lambda A_5(x), \tag{3.12a}$$

$$\psi_5 = \lambda A_5(x)y^* \tag{3.12b}$$

with

$$A_5\left(0^+\right) = A_4(\infty), \tag{3.12c}$$

to match to the behaviour in sublayer 4, and the pressure response $p_5(x)$ is unknown. The overbody condition of tangential flow then yields

$$A_5(x) = -f^+(x) + f^+(0) + A_4(\infty), \tag{3.12d}$$

with allowance made for $f^+(x)$ being nonzero at $x = 0^+$. The pressure–displacement law (2.2h) now acts to determine the induced pressure difference between the overbody surface and the upper

channel wall explicitly as

$$p_5(x) - \hat{p}(x) = Jf^{+\prime\prime}(x), \tag{3.12e}$$

since $p_5(x) - \hat{p}(x)$ is in balance with $-JA_T^{*\prime\prime}(x)$.

3.6 *The reduced problem*

The results (3.12d), (3.12e) hold throughout $0 < x < L$. Also, the $O(1)$ pressure in sublayer 5 is comparable with that in sublayer 2 as well as being comparable with the pressure in the upper viscous wall layer.

Combining the results of sublayers 2, 5 and equating the values of the stream function ψ on the underbody and the overbody as mentioned earlier produces the following relation between the $K^{\pm}$ values,

$$\lambda y_0^* K^- = -\pi_T^*/\lambda + \lambda y_0^* K^+. \tag{3.13}$$

The lower sublayers 1, 2 are insulated in effect from the extra region 4. We also have (3.10c), however. Hence the displacement effect acting on the lowest sublayer 1 is given to within a constant as

$$A_2(x) = -f^-(x) + f^+(0) + \left[A_0 + \pi_T^*/\left(\lambda^2 y_0^*\right)\right]. \tag{3.14}$$

The result (3.14) determines the displacement that helps to drive the flow in the lowermost viscous layer 1 by means of the condition (3.3b) but subject to guessed values of A_0, π_T^* and the prescribed y_0^* value of unity for the leading edge height. The result (3.14) when applied at $x = 0^+$ also confirms that, in (3.1), the coefficient

$$\pi_T^* = \lambda^2 \left[A_2 \left(0^+\right) - A_0\right], \tag{3.15}$$

since $f^+(0) = f^-(0)$ and $y_0^* = 1$. The earlier behaviour in (2.8b) ties in with this coefficient. Our reduced problem is given by (2.2a)–(2.2h) in essence subject to a displacement set by $A_2(x)$ in (3.14) holding in the gap between the body and the wall, with unknown constants representing the unknown mass flux entering the gap. Crucially, we see that linearisation is now possible, allowing a way in to analytical progress.

4. Linearised behaviour: effects of body thickness

With the physical influences of position, length and thickness in mind, linearised properties are sought as a first step in understanding the behaviour of the complete fluid–body system. This continues on from section 3 but for body shapes

$$f^{\pm}(x) = \epsilon f^{(1)\pm}(x) \tag{4.1}$$

with the typical relative thickness factor ϵ being small and the scaled shape functions $f^{(1)\pm}(x)$ being of order unity. The major mechanical interactions take place in the region upstream of the body (upstream influence), in the gap (direct body-shape effects) and in the region downstream of the body (downstream influence). In the nonlinear regime, within the upstream region the full equations (2.2a)–(2.2c), (2.2g), (2.2h) control the nonlinear free interaction for $x < 0$, without the $y = F^{\pm}(x)$ condition but with boundedness far upstream; in the gap (2.2a)–(2.2e) hold without the $y = F^{\pm}(x)$ condition but with an effective $A(x)$ specified to within a constant as in (3.14); in the downstream region (2.2a)–(2.2c), (2.2g), (2.2h) apply again without the $y = F^{\pm}(x)$ condition but with boundedness far downstream; the problem remains a largely numerical one then. In the

linearised regime by contrast considerable progress is possible analytically as follows. Subsection 4.1 addresses the details of the flow solutions in the different regions and subsection 4.2 then tackles the linearised interaction.

4.1 *Details of the flow solutions*

Expanding in powers of ϵ in the upstream and downstream wall layers $x < 0$, $x > L$ in turn as well as in the $O(1)$ wall layers occupying $0 < x < L$ we have

$$(u, v, p, A) = (\lambda y, 0, 0, 0) + \epsilon \left(u^{(1)}, v^{(1)}, p^{(1)}, A^{(1)}\right) + \cdots, \tag{4.2a}$$

$$\left(\hat{u}, \hat{v}, \hat{p}\right) = \left(\lambda\hat{y}, 0, 0\right) + \epsilon \left(\hat{u}^{(1)}, \hat{v}^{(1)}, \hat{p}^{(1)}\right) + \cdots, \tag{4.2b}$$

and likewise in the (u_1, v_1, p_1) layer of (3.3a)–(3.3c) with (2.4), (3.14). The superscript (1) denotes perturbation quantities throughout. The governing equations (2.2a)–(2.2c) in the lower wall layer ahead of and downstream of the body now become,

$$u_x^{(1)} + v_y^{(1)} = 0, \; \lambda y u_x^{(1)} + v^{(1)}\lambda = -p^{(1)\prime}(x) + u_{yy}^{(1)}, \tag{4.3a}$$

$$u^{(1)} = v^{(1)} = 0 \text{ at } y = 0, \tag{4.3b}$$

$$u^{(1)} \to \lambda A^{(1)} \text{ as } y \to \infty, \tag{4.3c}$$

while in the upper wall layer ahead of and downstream of the body the same equations hold for $\hat{u}^{(1)}$, etc., apart from the condition (4.3c) which is replaced by

$$\hat{u}^{(1)} \to -\lambda A^{(1)} \text{ as } \hat{y} \to \infty. \tag{4.4a}$$

In the lower wall layer underneath the body we have, from (3.2) and (3.3), the same system (4.3) applying for $(u_1^{(1)}, v_1^{(1)}, p_1^{(1)})$ except that

$$u_1^{(1)} \to \lambda A_2^{(1)} \text{ as } y \to \infty, \tag{4.4b}$$

which confirms the continuation with (4.3) along the lower wall. In the upper wall layer above the body the system (4.3) again holds for $\hat{u}^{(1)}$, etc., for the length scale x of $O(1)$ but with

$$\hat{u}^{(1)} \to -\lambda A_5^{(1)} \text{ as } \hat{y} \to \infty. \tag{4.4c}$$

Here the right-hand sides of (4.4b), (4.4c) are given in effect by (3.14), (3.12d), respectively with superscript (1) where we note that the adjustment form (3.6) acts over a short length scale to smooth out the flow solution in order to satisfy the condition (2.6). In addition, the pressure–curvature relation retains the form (2.2h) ahead of and behind the body with superscript (1) inserted, whereas over the body we have (3.12e), again with superscript (1) inserted. The main continuity or jump conditions across the leading edge $x = 0^{\pm}$ in (2.2d) are now as follows:

$$p_2^{(1)} = \pi_0^{(1)} \text{ at } x = 0, \tag{4.5a}$$

$$A_5^{(1)}\left(0^+\right) - A_0^{(1)} = A_2^{(1)}\left(0^+\right) - A_0^{(1)} = \pi_T^{*(1)}/\left(\lambda^2 y_0^*\right). \tag{4.5b}$$

The axial continuity of pressure in (4.5a) stems from (2.7) after linearisation since the velocity contribution is then small. The axial discontinuity in displacements across the leading edge station in (4.5b) is implied by the linearised versions of (3.12d), (3.14) given that the perturbed shape values $f^{(1)\pm}(0)$ must be equal. The trailing edge condition of equal pressures in (2.2e), (2.9) becomes

$$p_5^{(1)} = p_2^{(1)} \text{ at } x = L, \tag{4.5c}$$

and the boundedness requirement as $x \to \pm\infty$ in (2.2f) is essentially that of no exponential growth upstream and downstream.

4.2 *The linearised interactive problem*

In view of the cross-channel relations (2.2h), (3.12e) with superscripts (1) present we treat the system (4.3)–(4.5) by using difference variables defined as

$$[U, P, B] = \left[\hat{u}^{(1)} - u^{(1)}, \hat{p}^{(1)} - p^{(1)}, -\lambda\left(A^{+(1)} + A^{-(1)}\right)\right], \tag{4.6}$$

upstream and downstream of the body where $A^{+(1)}, A^{-(1)}$ are the negative displacements at the upper and lower wall layers in turn and similarly for the body range where B is $-\lambda(A_5^{(1)} + A_2^{(1)})$, while P is $p_5^{(1)}(x) - p_2^{(1)}(x) - Jf^{+(1)''}(x)$. Then subtracting the lower- from the upper-wall balances we obtain for the difference variables

$$U = \Psi_y, \quad V = -\Psi_x, \quad \lambda Y U_x + V\lambda = -P_x + U_{yy}, \tag{4.7a}$$

$$U = V = 0 \text{ at } y = 0, \tag{4.7b}$$

$$U \to B(x) \text{ as } y \to \infty. \tag{4.7c}$$

From the mixed requirements on the flow solution the conditions on P, B here are

$$P = -(J/2\lambda)B_{xx} \text{ for } x < 0, x > L, \text{ with } P, B \text{ unknown}, \tag{4.8a}$$

$$B(x) = 2\lambda\left[\left(f^{+(1)}(x) + f^{-(1)}(x)\right)/2 - f(0) - A_0^{(1)} - \pi_T^{*(1)}/\left(\lambda^2 y_0^*\right)\right]$$

$$\text{for } 0 < x < L, \text{ with } P \text{ unknown}. \tag{4.8b}$$

The condition (4.8a) represents free-interaction effects (**24**–**26**). In (4.8b), the shapes $f^{\pm(1)}(x)$ and height y_0^* are specified, typically $y_0^* = 1$, and $f^\pm(0) = f(0)$. If pressures $\pi_0^{*(1)}$ (and hence displacement $A_0^{(1)}$), $\pi_T^{*(1)}$ are also known or guessed then (4.8b) represents a condensed-flow configuration in which the effective displacement is given and the effective pressure is to be found. The latter determines the pressure difference acting normally across the body by virtue of the definition of P prior to (4.7).

The solution of (4.7), (4.8) is obtained in the next section. We notice that the conditions across the leading edge station now have the effective pressure P being continuous but the effective displacement B, which is to satisfy the jump condition

$$B\left(0^+\right) - B\left(0^-\right) = -2\pi_T^{*(1)}/\left(\lambda y_0^*\right), \tag{4.9}$$

is discontinuous in general.

5. Solution properties: effects of body shape

The aim here is to determine the size of the upstream influence factor and the pressure and displacement responses (and subsequently to determine the free motion of the body). Subsection 5.1 considers a fundamental case having a comparatively simple shape of body which represents a basic model of an ice shard for example as discussed in our introduction. Subsection 5.2 then brings the multi-structured solution together.

5.1 A central case

The current quasi-steady properties are quite dependent on body shape. So we take a basic case primarily. This corresponds to a general body shape at increased angle of rotation and relative height, however, while if instability ensues in the unsteady regime then that basic case is found to dictate the instability (1, 2).

The central case of a thin straight body at incidence is addressed below, such that

$$f^{+(1)}(x) = f^{-(1)}(x) = h + (x - L/2)\,\theta \tag{5.1}$$

where the prescribed constant h is a height factor for the body position and the prescribed constant θ describes the inclination. In this case, the effective displacement in (4.8b), with K denoting the unknown constant $f(0) + A_0^{(1)} + \pi_T^{*(1)}/(\lambda^2 y_0^*)$ and $f(0) = h - L\theta/2$, becomes

$$B(x) = 2\lambda\,[h + (x - L/2)\,\theta - K]\ \text{for } 0 < x < L. \tag{5.2}$$

The unknown effective pressure P is $p_5^{(1)}(x) - p_2^{(1)}(x)$ since the curvature $f^{(1)+\prime\prime}(x)$ is identically zero in the current case. We may also normalise λ, J, θ to unity or indeed to any values without loss of generality. The normalisation is by putting $x = x_1\bar{x}$, $U = U_1\bar{U}$ (etc.) with the coefficients for given λ, J, θ being $x_1 = J_1^{3/7}\lambda^{-5/7}$, $y_1 = J_1^{1/7}\lambda^{-4/7}$, $P_1 = J_1^{1/7}\lambda^{3/7}B_1$, $\theta_1 = J_1^{-3/7}\lambda^{-2/7}B_1$, $(h_K)_1 = \lambda^{-1}B_1$, $U_1 = B_1$, $L_1 = x_1$ where the unknown constant h_K stands for $h - K$, and then working in terms of the barred quantities. (In fact we keep (λ, J, θ) as factors in the analysis as stated earlier, while setting them as $(1, 1/30, 1)$ in most of the eventual numerical working.)

The solution of (4.7), (4.8a) for the upstream range $x < 0$ is given by an exponential eigenfunction such that (24, 25)

$$P(x) = -\,(J/2\lambda)\,G\kappa^2\exp\,(\kappa x)\,,\ B(x) = G\exp\,(\kappa x), \tag{5.3}$$

with the coefficient G to be determined. The eigenvalue $\kappa = [-6\mathrm{Ai}'(0)/J]^{3/7}\lambda^{5/7}$ which for (λ, J) of $(1, 1/30)$ gives κ as 5.18766 approximately.

For the range $0 < x < L$ in which, to repeat, we can suppose P to be continuous across $x = 0$ and allow B to be discontinuous there due to (4.9), a transform approach (25) leads to the parabolic result

$$P(x) = -\,(\gamma/\lambda)\left[Gx^{1/3}\int_0^\infty \exp\,(-\kappa xv)\,(1 + v)^{-2/3}\ \mathrm{d}v\right.$$
$$\left. +\,2\lambda\int_0^x [h_K + (s - L/2)\,\theta]\,(x - s)^{-2/3}\ \mathrm{d}s\right], \tag{5.4}$$

from (5.2). The constant $\gamma = -3\mathrm{Ai}'(0)\lambda^{5/3}/\Gamma(1/3) = 0.289838\lambda^{5/3}$. The value of h_K is to be determined such that $\alpha(L^-) = 0$ to accommodate the Kutta condition at the trailing edge.

For the downstream range, where $x > L$, free interaction returns to play and yields the coupling of the relation (4.8a) with

$$P(x) = -(\gamma/\lambda)\left[\alpha(x) + \int_L^x B(s)(x-s)^{-2/3}\,\mathrm{d}s\right], \tag{5.5a}$$

where

$$\alpha(x) = Gx^{1/3}\int_0^\infty \exp(-\kappa xv)(1+v)^{-2/3}\,\mathrm{d}v + 2\lambda\int_0^L [h_K + (s-L/2)\,\theta](x-s)^{-2/3}\,\mathrm{d}s. \tag{5.5b}$$

Hence the displacement function $B(x)$ satisfies the ordinary differential equation

$$(J/2\gamma)B_{xx} = \alpha(x) + \int_L^x B(s)(x-s)^{-2/3}\,\mathrm{d}s, \tag{5.6a}$$

for all $x > L$. The starting conditions at $x = L^+$ are B, B_x to be continuous and $B_{xx} = 0$ for, in turn, continuity of displacement, its slope and the pressure at the trailing edge. So

$$B(L^+) = 2\lambda[h_K + (L/2)\,\theta], \tag{5.6b}$$

$$B_x(L^+) = 2\lambda\theta, \tag{5.6c}$$

$$B_{xx}(L^+) = 0. \tag{5.6d}$$

The task now is to solve (5.6) to find the constant G such that P, B avoid exponential $(\exp(\kappa x))$ growth far downstream, leaving only algebraic decay there. The condition (5.6d) is actually satisfied by $\alpha(L^-) = 0$ together with $\alpha(X)$ assumed

5.2 *Assembling the flow solution*

A Laplace transform is applied to calculate the final solution combined with a splitting of the function $\alpha(x)$ in (5.5b) as $\alpha(X) = G\alpha_1 + 2\lambda[h_K\alpha_{21} + \alpha_{22}]$ where, with $Z = (x-L)$,

$$\alpha_1 = x^{1/3}\int_0^\infty \exp(-\kappa xv)(1+v)^{-2/3}\,\mathrm{d}v \tag{5.7a}$$

$$\alpha_{21} = 3\left(x^{1/3} - Z^{1/3}\right), \tag{5.7b}$$

$$\alpha_{22} = 3\theta\left[-(3/4)Z^{4/3} - (1/2)LZ^{1/3} + (3/4)x^{4/3} - (1/2)Lx^{1/3}\right]. \tag{5.7c}$$

The coefficients $\alpha_1, \alpha_{21}, \alpha_{22}$ are independent of G, h_K. The right-hand side of (5.7a) is readily computed. Then the above requirements $\alpha(L) = 0$ and zero residue in Laplace-transform space in order to prevent any $\exp(\kappa x)$ growth at large positive x imply the results

$$G\alpha_1(L) + 2\lambda h_K\alpha_{21}(L) + 2\lambda\alpha_{22}(L) = 0, \tag{5.8a}$$

$$GT_1 + 2\lambda h_K T_{21} + 2\lambda T_{22} = -2\lambda e_1[\kappa h_K + (1 + \kappa L/2)\,\theta] \tag{5.8b}$$

with

$$T_n = \int_L^\infty \alpha_n(x) \exp\left[-\kappa(x-L)\right] dx. \tag{5.8c}$$

Here, $e_1 = J/(2\gamma) = 0.057034$ and $\kappa = [\Gamma(1/3)/e_1]^{3/7} = 5.18766$ (again) are known constants. Hence two explicit linear equations $q_1 G + 2q_2\lambda h_K = 2\lambda q_3$ and $q_4 G + 2q_5\lambda h_K = 2\lambda q_6$ apply, giving (for those readers interested in detail)

$$G = 2\lambda \left(q_5 q_3 - q_2 q_6\right)/D, \ h_K = \left(q_1 q_6 - q_4 q_3\right)/D, \ \text{with } D = q_5 q_1 - q_2 q_4 \tag{5.9a}$$

where

$$\left[q_1, q_2, q_3, q_4, q_5, q_6\right] = \left[\alpha_1(L), \alpha_{21}(L), -\alpha_{22}(L), T_1, T_{21} + e_1 H, -T_{22} - e_1 \left(1 + HL/2\right)\theta\right]. \tag{5.9b}$$

The values G, h_K above determine the solution throughout the flow field for any θ value. From these solution values the pressure P and displacement B in particular can be obtained from (5.3) and so on.

That completes the linearised solution then. The solution curves of G, h_K against L are presented in Fig. 6. We used both finite-difference calculations and analytically based calculations to determine the solutions and the results from the two calculations agreed. The analytical ones as implemented tended to yield the whole solution faster. Both the upstream-influence factor G and the height factor h_K are monotonic functions of the length L of the body.
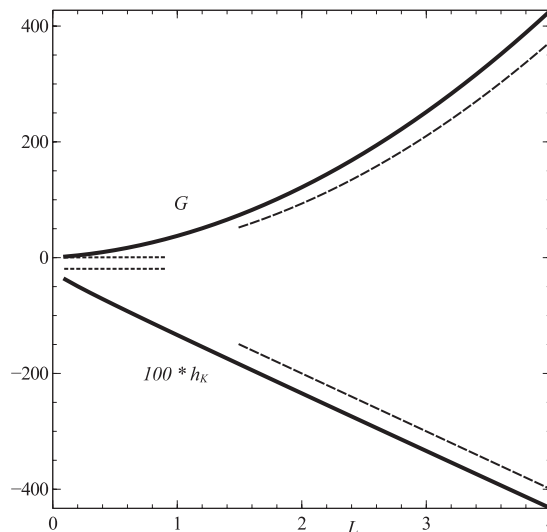
Fig. 6 Investigating the effects of body length: dependence of the upstream-influence factor G and height factor h_K on the scaled body length L. Here, $(\lambda, J) = (1, 1/30)$ and inclination $\theta = 1$. The thinner curves with small and large dashes indicate the asymptotes for small and large values of L, respectively.

Extreme values of the body length factor L are of interest to help complete our understanding. At small values of L the equations (5.8) show that

$$G \sim G_1 L^{1/3} \theta \, (\to 0) \text{ and } h_K \to h_{K0} \theta \, (\sim 1), \text{ for } L \ll 1, \tag{5.10}$$

where the constants are $G_1 = 6\lambda/[\Gamma(1/3)\kappa^{2/3}]$, $h_{K0} = -1/\kappa$. The argument for large values of L follows similar lines and is such that after some working we find from (5.8), (5.9) the asymptotes

$$h_K \sim -L\theta \text{ and } G \sim (9\lambda\kappa/2) L^2 \theta, \text{ for } L \gg 1, \tag{5.11}$$

to leading order. These asymptotes are seen to be in close agreement with the computational results for increasing L values in Fig. 6 and indeed they even give a fair approximation for L of unity. The more physical implications for both small and large L values are presented in the next section.

6. Effects of body length

We discuss the implications for shorter bodies and longer bodies in subsections 6.1 and 6.2 below. The only previous studies are by references (**1**, **2**), respectively which included significant assumptions over the disparate length scales present as well as placing the typical thin body within the core of the fluid motion. There is a need to examine the match of the present flow solutions with the previous ones, given the new information from the present study and the importance of length effects as well as position and thickness.

6.1 *Shorter bodies*

The flow structure associated with decreased lengths L in section 5 has, first, a zone where x is $O(1)$ upstream of the body (zone 1) in which (5.3) still holds; second, a short zone where $x = L\hat{X}$ (zone 2) around the body for $-\infty < \hat{X} < \infty$ (the body occupies the interval $0 < \hat{X} < 1$); and third, a zone wherein x is of $O(1)$ again downstream (zone 3). The body is virtually horizontal on the length scale of $O(L)$ in the sense that

$$B = 2\lambda \left[h_{K0}\theta + L\left(\hat{X} - 1/2\right)\theta \right] \sim 2\lambda h_{K0}\theta, \text{ to leading order}, \tag{6.1}$$

and the result (6.1) continues to apply throughout the wake over the $O(L)$ length scale. The wake remains virtually straight and only slightly inclined by the small but growing θ effect in (6.1). We repeat that B is discontinuous at the leading edge. The trailing edge condition on pressure is satisfied due to B simply carrying on almost straight there; B only deviates once the $O(1)$ length in x is encountered relatively far downstream where the $\hat{X}\theta$ contribution increases to overtake $h_{K0}\theta$. The above provides the only forcing on the $O(1)$-wake length scale. Thus there we have (5.6a) but with α, L now replaced by zero in effect and, given (5.6d) is automatically satisfied, the starting conditions become

$$B\left(0^+\right) = 2\lambda h_{K0}\theta, \; B_X\left(0^+\right) = 2\lambda\theta. \tag{6.2}$$

Finiteness as $x \to \infty$ then requires $h_{K0} = -1/\kappa$ as per (5.8b), thereby confirming the form of h_{K0} in (5.10). Meanwhile, on the short $O(L)$ body scale the result (5.4) yields p of $O(L^{1/3})$, specifically

$$p\left(\hat{X}\right) = -(\gamma/\lambda) L^{1/3} \left[G_1 \hat{X}^{1/3} \Gamma(1/3)\kappa^{-1/3} + 2\lambda h_{K0} \int_0^{\hat{X}} \left(\hat{X} - \hat{s}\right)^{-2/3} \mathrm{d}\hat{s} \right]. \tag{6.3}$$

Hence the constraint of zero p at the trailing edge requires

$$G_1 \Gamma(1/3)\kappa^{-1/3} + 2\lambda h_{K0} \int_0^1 (1 - \hat{s})^{-2/3} \, \mathrm{d}\hat{s} = 0,$$

giving

$$G_1 \Gamma(1/3)\kappa^{-1/3} = -6\lambda h_{K0}. \tag{6.4}$$

The left-hand side in (6.4) is from the pressure rise (or fall) because of the lengthy upstream influence ahead of the body, involving pressure–displacement interplay, whereas the right-hand side comes from the pressure fall (or rise) because of the fixed-displacement effect over the shortened length scale of the body itself. The finding (6.4) confirms the form of G_1 in (5.10). The pressure-difference curve p consists of a slow exponential growth upstream followed by a fast drop to zero at $\hat{X} = 1$. Zones 1, 3 have p, B both being of order $L^{1/3}$ with x of $O(1)$ by virtue of the free interaction upstream and downstream, while zone 2 has p, B of order $L^{1/3}$ (except in the lower near-wake p) with the length scale $x \sim L$ being small there.

We may now reconsider the Reynolds number effect as well. The prime interpretation here, concerning a body of length comparable with the channel width and sited inside the core of the flow, to compare with other work, follows from the small-L limit above by letting L become as small as $\mathrm{Re}^{-1/7}$ in view of the original expansions in section 2. Also, however, the enlarged height parameter H of section 3 plays a role since now H tends to the order of $\mathrm{Re}^{2/7}$. The double limit process implies an $O(\mathrm{Re}^{1/7} a_D)$ length of upstream influence and downstream influence for a body of length comparable with the channel width a_D; moreover, the three zones upstream, downstream and surrounding the body from 1 to 3 above couple nontrivially as indicated in section 5. The sole change occurs in the body zone 2 due to a Laplacian-like balance operating when the body length becomes $O(a_D)$. Along with that the additional axial length scaling of $H^{-1/2}$ that takes place at large H in section 3 leads to the same axial $O(a_D)$ stage when the body enters the core.

The scalings and flow structure in this shorter-body scenario comply with those in (**1**), and the details of the increased-length cases in that reference confirm those implied in the previous paragraph, thus providing a direct match. Hence the assumptions made in (**1**) about longer-scale effects arising in the presence of a relatively short body are justified by the present study. Further, for a body of length between $O(a_D)$ and $O(\mathrm{Re}^{1/7} a_D)$ and negligible thickness the solution in (5.10), (6.1)–(6.4) applies throughout.

6.2 *Longer bodies*

Likewise at large values of L the pressure response in (5.4) shows more than one spatial scale. For x of $O(1)$ the first term on the right dominates, giving an $O(L^2\theta)$ contribution in view of G in (5.11) in contrast with the $O(L\theta)$ contribution from the second term under the assumption of (5.11) for h_K. Over the majority of the body where x is of $O(L)$ the first and second terms are both of order $L^{4/3}\theta$. Thus the flow structure and the order of magnitude of the pressure agree with those in (**2**) for longer bodies. In particular, the pressure scaling of $L^{2/3}$ in (**2**) over the body scale matches with the present finding since the representative height and length factors are $L^{1/3}$, L, respectively as L increases, making the inclination θ reduce like $L^{-2/3}$ typically.

A distinction here is that the pressure does pick up an effect which grows like $X^{-2/3}$ at small X ($= x/L$), nearer the leading edge, due to the first term in (5.4) which corresponds to an effect from upstream influence as G is involved directly. This means that, at least over some parameter ranges,

the Kutta condition at the trailing edge of the body may have more impact than suggested in the above article because of the singular behaviour admitted nearer the leading edge, an aspect which remains to be studied in detail. The pressure at $O(1)$ distances here in terms of x from the leading edge has the $L^{4/3}$ scaling, given the θ scaling above.

7. Free movement of the body

Evolution with time can be incorporated. One way is through quasi-steady flow interacting with unsteady body movement for large density ratios as in (**1**, **2**). In that scenario, the nonlinear system of section 2 remains intact with slow time dependence present but this is coupled with the body-motion balances

$$M\frac{d^2 h}{dt^2} = \int_0^L \left(p^- - p^+\right)(x, t)\,\mathrm{d}x, \tag{7.1a}$$

$$I\frac{d^2\theta}{dt^2} = \int_0^L (x - L/2)\left(p^- - p^+\right)(x, t)\,\mathrm{d}x. \tag{7.1b}$$

Here M, I are the scaled mass and moment of inertia of the body and h, θ are the unknown scaled displacement of and rotation angle about the centre of mass, respectively similar to the effects in section 5. The overbody is subjected to the pressure p^+, while p^- acts on the underbody. The centre of mass is assumed to be at the midpoint of the body. Now the moving body surfaces take the forms

$$F^{\pm}(x, t) = F_1^{\pm}(x) + h(t) + (x - L/2)\theta(t), \tag{7.1c}$$

however, with the shapes $F_1^{\pm}(x)$ independent of the scaled time t but the leading edge height H now varying in time. The unknown pressure differences in (7.1a), (7.1b) thus drive the body movements laterally and rotationally. The body movement axially remains negligible by comparison (**1**, **2**).

One notable feature concerns the influence on (7.1a), (7.1b) when H becomes large. The paramount contributions in this regime come from the shortened region 4 of section 3 where the relatively large pressure (see Figs 4 and 5) provokes the largest force and moment present. Linearising as in section 4 and then using an unknown constant Q for the time derivative as in (**1**, **2**) with exponential dependence $\exp(Qt)$ leads to $Q^2 Mh$, $Q^2 I\theta$ on the left-hand sides in (7.1a), (7.1b). The second equation determines Q and then the first determines $h(t)$. Working with region 4 of section 3 indicates that positive θ, where $G, \pi_T^{*(1)}, \pi_T^*$ are also positive, implies a positive p_4 from (3.10a) and hence a positive $\mathrm{d}^2\theta/\mathrm{d}t^2$ or Q^2 from (7.1b). Specifically, we find the growth rate Q to be determined by

$$Q^2 = H^{1/2}L\pi_T^* / \left(2q^* I\right), \tag{7.2}$$

where the constants π_T^*, q^* defined in section 3 and the moment of inertia I are all positive. In consequence instability is induced (cf stabilisation measures in (**2**)). This agrees with the findings in (**1**, **2**) with the focus in the latter case on (viscous) effects independent of lateral position being abetted by the present (inviscid) effects that do depend on lateral position. In particular, the growth rate Q decreases as the 1/4 power of distance from the wall.

8. Conclusions

Here, in concluding, we address several follow-on issues and possible future prospects, noting in addition that practical examples are described in Appendix A.

Immediate follow-on points of note are as follows. First, the difficult nonlinear problems posed originally in sections 2 and 3 should be of much interest in view of the linearised findings here. These findings establish that the intricate problems of combined fluid and body motion over a wide range of settings are closed and the analytical solutions will act as a guide for nonlinear case studies. Second, two limit processes are coupled in the above subsections, namely scaled height H increasing and length scale L decreasing or increasing depending on the particular case of concern. Letting H alone increase instead leads to the flow structure for a body of interactive length $O(\mathrm{Re}^{1/7}a_D)$ resident in the core. Here, the nonlinear system of section 2 applies in each wall layer but with the pressure–curvature interaction holding only ahead of and behind the body, whereas the wall layers beneath and above the body are subjected to conditions analogous to those in sections 3 and 4. This represents another interesting nonlinear stage. The matching should tend to agree with the flow structures in the earlier studies (**1**, **2**) as body length is varied. Third, we would re-emphasise the effects of upstream and downstream influence which are clarified by the present crossover (1/7) case with its rather subtle structuring of the flow solution and the distinctions between short and long scale interactions. Fourth is the importance of the local short-scaled Euler zone near the leading edge of the body (see section 2), as it yields properties in the current interactive-length case that produce (see section 3) an interesting and unexpected short-length flow structure as scaled heights H become large.

Future study may include the following points (a–f). (a) Future work should tackle the nonlinear versions of sections 2 and 3 as well as that mentioned in the first paragraph of the present subsection. Essentially, the same problem is found for a wall jet as regards the linearised properties and solutions of sections 4 and 5. (b) The current study yields interesting and sensitive flow structures when the body resides near a channel wall and extra contributions to lift and moment on the body. The double limits of small length L with large height H and of large L with large H need to be investigated further to fill in more of the parametric dependence. (c) The implications for an external boundary layer setting merit exploration; this case is likely to be analogous to the present one but with the behaviour in region 4 of section 3 being significantly different. (d) Another way for unsteadiness to enter play is through the fluid flow equations rather than (7.1a), (7.1b) and potentially this admits classical channel flow instabilities (**25**, **26**), contrasting with the non-classical instability (**1**, **2**) in (7.1a), (7.1b). (e) Implications exist possibly for branching and reconnecting flows. (f) The axial velocity of the body has been taken as negligibly small throughout, an assumption which could be relaxed as in the above two references. Similarly, it would seem beneficial to venture further into parameter space regarding the effects of many bodies and of three spatial dimensions for instance.

References

1. F. T. Smith and E. R. Johnson, Movement of a finite body in channel flow, *Proc. Roy. Soc. A*, **472** (2016) 20160164.

2. F. T. Smith, Free motion of a body in a boundary layer or channel flow, *J. Fluid Mech.* **813** (2017) 279–300.

3. S. Mettu, N. Verma and R. P. Chhabra, Momentum and heat transfer from an asymmetrically confined circular cylinder in a plane channel, *Heat Mass Transf.* **42** (2006) 1037–1048.

4. M. Sahin and R. G. Owens, A numerical investigation of wall effects up to high blockage ratios on two-dimensional flow past a confined circular cylinder, *Phys. Fluids* **16** (2004) 1305–1320.

5. B. Kumar and S. Mittal, Effect of blockage on critical parameters for flow past a circular cylinder, *Int. J. Numer. Methods Fluids* **50** (2006) 987–1001.

6. F. Rehimi, F. Aloui, S. B. Nasrallah, L. Doubliez and J. Legrand, Experimental investigation of a confined flow downstream of a circular cylinder centred between two parallel walls, *J. Fluids Struct.* **24** (2008) 855–882.

7. A. G. Kidanemariam, C. Chan-Braun, T. Doychev and M. Uhlmann, Direct numerical simulation of horizontal open channel flow with finite-size, heavy particles at low solid volume fraction, *New J. Phys.* **15** (2013) 025031.

8. V. Loisel, M. Abbas, O. Masbernat and E. Climent, The effect of neutrally buoyant finite-size particles on channel flows in the laminar-turbulent transition regime, *Phys. Fluids* **25** (2013) 123304.

9. A. J. C. Ladd, Numerical simulations of particulate suspensions via a discretized Boltzmann equation. Part 1. Theoretical foundation, *J. Fluid Mech.*, **271** (1994) 285–309.

10. F. T. Smith, S. Balta, K. Liu and E. R. Johnson, On dynamic interactions between body motion and fluid motion, Mathematics Applied to Engineering, Modelling and Social Issues (ed. F. T. Smith, H. Dutta, J. N. Mordenson; Springer Nature Switzerland 2019).

11. F. T. Smith and A. S. Ellis, On interaction between falling bodies and the surrounding fluid, *Mathematika* **56** (2010) 140–168.

12. F. T. Smith, Fluid-body interactions: clashing, skimming, bouncing, *Philos. Trans. R. Soc. A Math. Phys. Eng. Sci.* **369** (2011) 3007–3024.

13. P. D. Hicks and F. T. Smith, Skimming impacts and rebounds on shallow liquid layers, *Proc. R. Soc. A* **467** (2011) 653–674.

14. F. T. Smith and K. Liu, Flooding and sinking of an originally skimming body, *J. Eng. Math.* **107** (2017) 37–60.

15. F. T. Smith and P. L. Wilson, Body-rock or lift-off in flow, *J. Fluid Mech.* **735** (2013) 91–119.

16. S. Balta, *On fluid-body and fluid-network interactions*. Ph.D. Thesis (University College London 2017).

17. L.-P. Wang, M. R. Maxey, T. D. Burton and D. E. Stock, Chaotic dynamics of particle dispersion in fluids, *Phys. Fluid Fluid Dynam.* **4** (1992) 1789–1804.

18. N. T. Ouellette, P. J. J. O'Malley and J. P. Gollub, Transport of finite-sized particles in chaotic flow, *Phys. Rev. Lett.* **101** (2008) 174504.

19. T. P. Sapsis, N. T. Ouellette, J. P. Gollub and G. Haller, Neutrally buoyant particle dynamics in fluid flows: comparison of experiments with Lagrangian stochastic models, *Phys. Fluids* **23** (2011) 093304.

20. R. Ni, S. Kramel, N. T. Ouellette and G. A. Voth, Measurements of the coupling between the tumbling of rods and the velocity gradient tensor in turbulence, *J. Fluid Mech.* **766** (2015) 202–225.

21. K. Wu, D. Yang, N. Wright and A. Khan, An integrated particle model for fluid-particle-structure interaction problems with free-surface flow and structural failure, *J. Fluids Struct.* **76** (2018) 166–184.

22. F. T. Smith, N. C. Ovenden, P. T. Franke and D. J. Doorly, What happens to pressure when a flow enters a side branch? *J. Fluid Mech.* **479** (2003) 231–258.

23. S. Balta and F. T. Smith, Inviscid and low-viscosity flows in multi-branching and reconnecting networks, *J. Eng. Math.* **104** (2017) 1–18.

24. F. T. Smith, Upstream interactions in channel flows, *J. Fluid Mech.* **79** (1977) 631–655.

25. F. T. Smith, *Fluid and Solid Mechanics*, Chapter 5 (ed. S. Bullett, T. Fearn & F. Smith; World Scientific Publishing, London UK 2016).

26. F. T. Smith and R. J. Bodonyi, On the stability of the developing flow in a channel or circular pipe, *Q. J. Mech. Appl. Math.* **33** (1980) 293–320.

27. F. T. Smith, P. W. M. Brighton, P. S. Jackson and J. C. R. Hunt, On boundary-layer flow past two dimensional obstacles. *J. Fluid Mech.* **113** (1981) 123–152.

28. F. T. Smith and R. Palmer, A freely moving body in a boundary layer: nonlinear separated-flow effects, *J. Appl. Ocean Res.* **85** (2019) 107–118.

APPENDIX A

Practical examples

To recap, given the many firm practical reasons and motivations described in the section 1, it is perhaps somewhat surprising that little modelling of an applied-mathematical nature has been done previously in the subject of fluid–body interactions. It was felt by us to be desirable to try starting to fill that gap despite any apparent complexity in the subject. Our intent has been to make a beginning then, to tackle basic problems and to seek analytical guidance above all. We have found that complexity or at least delicacy does indeed arise in the study: in the case of a constriction in a channel there are only three main flow regions, the inviscid core and two viscous-inviscid wall layers, whereas in the present case of a detached body several more important regions come into play. On the other hand, concise analytical solutions have been derived for the body case, including influences of body position, thickness and length, and these findings can guide further study.

In terms of practical examples we still need to be cautious, we cannot be sure yet if practical use will ensue and we should not pretend that all regimes mentioned or not mentioned here are likely to be of practical relevance. Nevertheless let us consider a range of Reynolds numbers Re, say 10^2–10^3 depending on the particular application in mind, and apply the theoretical scalings. (A similar approach in (**24**) indicated close agreement with direct numerical simulations for a cornered channel flow.) Take H to be 2 for example and ϵ to be 0.3. Then the body length addressed is formally about 2–3 (from $\mathrm{Re}^{1/7}$) relative to the channel width of unity and the body thickness is about 0.1–0.25 (from $\mathrm{Re}^{-2/7}$), as is the wall-layer thickness. The ϵ factor reduces that thickness to 0.03–0.075 approximately for the linearised scenario, while laterally the body placement is at a distance of 0.2–0.5 (from $H\mathrm{Re}^{-2/7}$) from the channel wall. Further the limiting cases discussed in subsections 6.1, 6.2 for shorter and longer bodies, respectively adjust the length estimate to the range 1–6 approximately. Overall this theoretical configuration seems reasonably close to those relevant to a thin elliptical particle in blood flow or to an ice shard or other thin particle in aeroengine dynamics especially.

APPENDIX B

Numerical solution of the Euler flow

In regard to solving the Euler-flow equation (2.5) an iterative scheme is applied. The incoming velocity profile $u_E = u_0(y)$ is supposed given. Hence far upstream the corresponding stream function profile $\psi_E = \psi_0(y)$ can

be worked out through integration with respect to y, while the shear profile can be worked out by differentiation in y, yielding

$$\psi_0(y) \text{ and } f_E(y) \left\{= u'_0(y)\right\}. \tag{B.1}$$

Elimination of y between $\psi_0(y), f_E(y)$ in (B.1) therefore gives us the functional relation $f_E(\psi_0)$ and thus $f_E(\psi_E)$ throughout the Euler flow region since all streamlines are taken to emanate from far upstream. Suitable numerical interpolation is used on this relation at each stage.

Next a guess is made for ψ_E at every grid point (x_E, y) where $x_E = x_{E,-\infty} + (i-1)\Delta x_E, y = y_j = (j-1)\Delta y$ and $\Delta x_E, \Delta y$ are small uniform steps in the axial and lateral directions, respectively, the integer i runs from 1 to I and j runs from 1 to J. Here, $x_{E,-\infty}, x_{E,\infty}$ are the axial endpoints of the computational grid such that $x_{E,\infty} - x_{E,-\infty} = (I-1)\Delta x_E$ and I is the maximum value of i, while $y = y_\infty = (J-1)\Delta y$ represents the outer edge of the grid laterally. Then (2.5) is addressed schematically in the interior of the domain in a straightforward discretised form,

$$\frac{\psi_E(i-1,j) - 2\psi_E(i,j) + \psi_E(i+1,j)}{(\Delta x_E)^2} + \frac{\psi_E(i,j-1) - 2\psi_E(i,j) + \psi_E(i,j+1)}{(\Delta y)^2} = f_E(\psi_E(i,j)),$$
$$\tag{B.2}$$

where $\psi_E(i,j)$ now denotes the unknown numerical value at the typical grid point (i,j). The lateral boundary conditions are

$$\psi_E(i,1) = 0 \quad \text{for all } 1 \leq i \leq I, \tag{B.3}$$

$$\frac{\psi_E(i,J) - \psi_E(i,J-1)}{\Delta y} = y_\infty - \frac{\Delta y}{2} + A_0, \tag{B.4}$$

$$\psi_E(i,j_1) = C_E \quad \text{for } i_1 \leq i \leq I. \tag{B.5}$$

The constant A_0 is given and the incident shear λ is taken as unity. The integer i_1 signifies the starting position of the thin body which appears as an aligned flat plate in the present region, whereas j_1 fixes the local scaled gap width $(j_1 - 1)\Delta y = H$, and the constant C_E is the value of the scaled stream function on the body, a value which can be derived by iteration or in our case deduced directly from (2.8a) where the pressure difference $\pi_{\text{diff}} = \pi_G - \pi_0$ is prescribed. The conditions at the axial endpoints are imposed as

$$\psi_E(1,j) = \psi_0(y_j), \tag{B.6}$$

$$\psi_E(I,j) = \psi_G(y_j) \quad \text{for } 1 \leq j < j_1, \tag{B.7}$$

$$\psi_E(I,j) = \psi_T(y_j) \quad \text{for } j_1 + 1 \leq j \leq J-1, \tag{B.8}$$

in view of the incoming conditions upstream and the approach downstream to quasi-parallel flow in the gap and on top of the body in turn. The stream-function profiles on the right-hand sides in (B.7), (B.8) stem from lateral integration of the velocity profiles u_G, u_T, respectively.

The right-hand side of (B.2) is evaluated from the latest guessed value of ψ_E, and then at all interior points (B.2) is solved line by line throughout the domain, that is, at a given i the scheme solves for all $\psi_E(i,j)$ subject to (B.3)–(B.5), with $\psi_E(i-1,j), \psi_E(i+1,j)$ taking the latest iterated values. The procedure marches forward in i, applying (B.6)–(B.8) at the axial endpoints, updating the overall guesses ψ_E and revising the right-hand side of (B.2), and then repeatedly sweeping the domain until convergence is deemed to occur.

Typical values taken for $\Delta x_E, \Delta y, I, J$ were 0.025, 0.025, 201, 201, respectively for the case of $x_{E,\infty}, i_1, j_1$ equal to 2.5, 101, 33 in turn. The convergence criterion was that successive iterates for ψ_E should differ by less than 10^{-6} throughout the domain.